Nanoscale

Accepted Manuscript

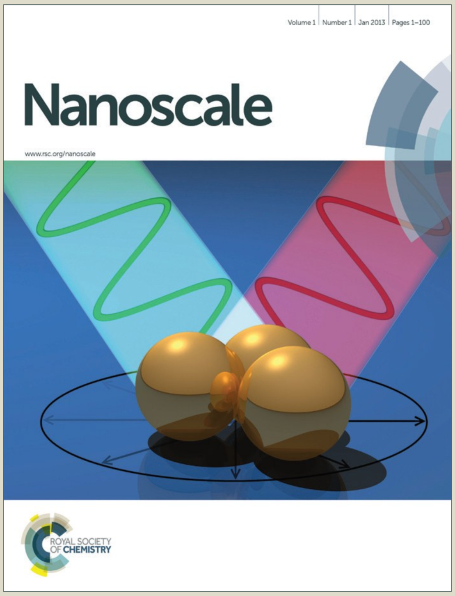

ROYAL SOCIETY OF CHEMISTRY

www.rsc.org/nanoscale

Nanoscale

ARTICLE

Non-templated ambient nanoperforation of graphene: A novel scalable process and its exploitation for energy and environmental applications

Received 00th January 20xx,
Accepted 00th January 20xx
DOI: 10.1039/x0

Suman Kumari Jhajharia, Kaliaperumal Selvaraj*

Received 00th January 20xx,
Accepted 00th January 20xx

DOI: 10.1039/x0xx00000x

www.rsc.org/nanoscale

Nano-perforation of 2D graphene sheets is a recent and strategically significant means to exploit them in modern applications such as energy production and storage. However, current options for the synthesis of holey graphene (hG) through nano-perforation of graphene involve industrially undesirable steps viz., usage of expensive/noble metal or silica nanoparticle templates and/or hazardous chemicals. This severely hampers its scope for large scale production and further exploitation. Here in, we report for the first time a scalable non-templated route to produce hG at perfectly ambient conditions. Nano-perforation is achieved with tunable pore size via a simple few layer co-assembly of silicate-surfactant admicelles along the surface of graphene oxide. A gentle alkali treatment and a reduction at optimized conditions readily yield holey graphene with a remarkable capacitance (~250 F g^{-1}) and interesting adsorption abilities for pollutants. Density functional theory based computational studies reveal interesting insight on the template free nano-perforation at molecular level. This simple rapid, process not only excludes the need of expensive templates and harmful chemicals to yield hG atattractively ambient, chemically placid and industrially safer conditions nevertheless leaves no hurdles towards scaling up.

Introduction

Graphene has attracted tremendous interest due to its unique physical and chemical properties ever since its discovery in 2004.[1] As a single layer of graphite, graphene features a perfect two-dimensional (2D) structure with a gamut of exceptional properties such as large specific surface area, high intrinsic carrier mobility,[2,3] strong mechanical strength,[4] and superior flexibility.[5] Starting from the famous scotch tape peeling of graphite,[6] several ways of making it have been found in literature; viz., chemical vapor deposition (CVD),[7] liquid phase exfoliation of graphite[8] and solution processing.[9,10] Except for the latter, other methods have limitation in the context of large scale production. Most solution routes simply involve aqueous exfoliation of graphene oxide (GO) and a reduction with hydrazine hydrate. Graphene is hence a front running carbon nanoform in energy applications due to this ease. Despite being an ideal electrical conductor, its zero band gap, easy and quick aggregation along with poor dispersion in common solvents limit its direct use in electro-catalysis and in energy storage devices. A tough to achieve but practically conflicting property match between larger surface area and a remarkable conductivity has been realized as a key means to turn graphene in to an unbeatable electrochemical material of future in energy applications. However, the past attempts towards achieving this balance with various possibilities and limitations are challenging. For example, one of the bottle neck is that free standing graphene sheets lose their large surface area (theoretically ∼2630 m^2 g^{-1}) while drying after an aqueous process as the retreating liquid meniscus reduces the spacing between the sheets resulting inrestacking.[11] Consequently, the effective utilization of their surface dramatically diminishes with reduction in porosity and ion diffusion across the sheets with large aspect ratios.[12] Although the introduction of oxygen containing functionalities between graphene sheets turning them in to graphene oxide (GO) sheets has brought little success, it pays heavily on its inherent high conductance.[13] Nonetheless, this imparts a dramatic boost to its dispersion in water and thus its existence in free form for further exploitation.

To solve the above issue, GO sheets can be converted back to graphene like material known as reduced graphene oxide (rGO) by chemical reduction or thermal annealing. Though this results, in a substantial revival of its electrical conductance, the chance of a quick re-stacking is an apparent risk. A surge of recent research reports focusing on this delicate equilibrium in novel materials for electrochemical, electronics and catalytic applications are hence explicable. Though higher dimensional carbon nanotubes (CNT) and fullerenes pretend to be understandably alternative materials to achieve this, graphene's hallmark conductance due to its long basal plane stands matchless before them. Hence, multidimensional structures of graphene are being explored. Attempts with different forms of them and their superstructures such as zero-dimensional (0D) graphene quantum dots, one-dimensional (1D) graphene nanoribbons and graphene fibers, two dimensional (2D) graphene films and three-dimensional (3D) graphene frameworks find wide applications in biomedicine, catalysis, imaging, photonics, quantum computing, sensing and even more.[14,15]

Nano and Computational Materials Lab., Catalysis Division,
CSIR-*National Chemical Laboratory, Pune-411008 India*

Phone (off.): +91-20-25 90 22 62, (Lab.): +91-20-25 90 22 79, Fax (off.): +91-20-25-90 26 33, E-mail: k.selvaraj@ncl.res.in; kselva@gmail.com

†Electronic Supplementary Information (ESI) available; See DOI: 10.1039/x0xx00000x

In this persistent run, two major kinds of graphene materials stand out: (i) self-assembled, macro-porous, 3D graphene structures (3DG) made using graphene sheets (with pore diameter >50 nm) and (ii) perforated graphene sheets known as holey graphene (hG) with meso-pores (diameter 2-50 nm) and micro-pores (diameter <2 nm). The 3DG structures are often made using hard templates such as polymer nanospheres,[16] metal or metal oxide nanoparticles[17,18] or using surface engineered substrates.[19,20] Thus, the large surface area and hydrophobicity of 3DG makes it the most employed porous carbon nanomaterial in recent years. Applications extend from water and air purification to molecular sieves and catalysts,[21] electrochemical devices, chromatographic separations,[22] energy, gas production and storage[23-25] and in nanoelectronics.[26]

On the other hand, holey graphene is synthesized by two distinct approaches viz., vapor phase and solution phase methods. Holey graphene structures obtained from lithographic methods (vapor phase) often referred to as "graphene nanomesh"[27-30] are technically unsuitable for large scale production due to the relatively lower yield and requirement of expensive infrastructure. In contrast, few more promising solution phase approaches are also reported. AuNP-mediated oxidation of rGO,[31] catalytic oxidation using Ag nanoparticles onto graphene sheets,[32] hierarchical perforations in GO sheets using Ludox solution followed by HF treatment and reduction[33] are a few examples under this class. Hence, hG has been reportedly possible with either noble metal NPs as hard templates or using acids such as HF thereby making the process unsafe for industrial exploitation. To the best of our knowledge, there is no report on nano-perforation of graphene without template or harmful acids at ambient conditions in literature. Hence, there is a fundamental aspiration to look for simple synthesis routes for hG production which are inexpensive, ambient and environmentally benign yet industrially promising.

Herein, we report for the first time, a uniquely rapid, scalable, industrially safer and yet simple route to produce hG. The process ensures no compromise on achieving high electrochemical capability of the hG by introducing nanoscopic in-plane large carbon vacancies (pores) using a few layer surface covering via sol-gel process followed by a minimal alkaline treatment to peel-off the silicate layer (illustrated in Scheme. 1). The process provides effortless tunability of pore diameter in the range few 10 to few 100 nm. Other positive aspects of this route in contrast to the reported ones are viz., avoidance of the (a) non-ambient conditions (b) non-aqueous medium (c) requirement of expensive noble metal / silica templates and (d) requirement of industrially hazardous acids such as HF. Few electrochemical investigations and sorption tests carried out on hG clearly prove its promising scope in applications such as energy storage/conversion, industrial pollutant removal of aquatic resources and possibly in scaffolding for catalysis and biosensing.

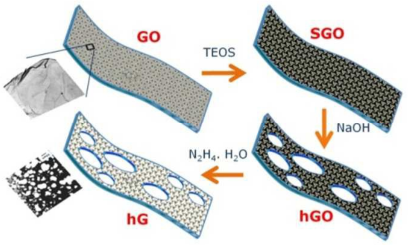

Scheme 1: A schematic of synthesis of holey graphene

Results and discussion

GO formation

GO, known to have –COH groups in the interlayer space and –COOH groups in the layer edges, is synthesized by modified Hummers method from graphite. A color change of graphite from black to clear brown after the said process implies the oxidation of carbon structure, which is verified by X-ray diffraction, UV-visible, FT-IR, solid state NMR and Raman spectroscopy. The XRD patterns as shown in Fig. 1A clearly indicate the formation of GO through a sharp peak at 10.76° for *002* plane with an associated d-spacing of 8.21 Å. The enlarged interlayer distance compared with pristine graphite (3.36 Å) is ascribed to the introduction of oxygen-containing functional groups on the surface of graphite due to oxidation.[34] Raman spectroscopy, a powerful tool to characterize especially the 2D carbon materials, is used to analyze both the samples (refer Fig. 1B). The graphite powder shows a prominent G line (related to the first-order scattering of E_{2g} mode) and a weak D line (related to the defect induced breathing mode of A_{1g} symmetry) with I_D/I_G ratio 0.44. The results prove the presence of higher degree of sp^2 carbon domains in graphite. After oxidation of graphite, GO displays two intensive bands viz; D and G at 1328 cm^{-1} and 1587 cm^{-1}, respectively with an I_D/I_G ratio of 0.9. A strong increment in I_D/I_G ratio (~ 0.46) on oxidation indicates a high degree of randomness compared to the original graphitic structure proving the successful functionalization.[35]

The UV-visible spectrum of GO (Fig. 1C) dispersion shows a main absorption peak centered at 230 nm and a weak shoulder around 300 nm, which are assigned to the π-π* transition of aromatic –C=C- and the n-π* transition proving the presence of non-bonding electrons on oxygen of carbonyl or carboxyl –C=O groups, respectively.[36] These results are in good agreement with the structural characteristics as observed in FT-IR results shown in Fig. 1D. While no significant peak is found in the FT-IR spectrum of the graphite, the presence of different types of oxygen functionalities in GO is confirmed by the adsorption bands corresponding to the O-H stretching at 3416 cm^{-1} and C=O carbonyl stretching at 1730 cm^{-1}. The band at 1625 cm^{-1} is assigned to the vibration of the adsorbed water molecules as well as to the contribution from the skeletal vibration of un-oxidized graphitic domains.[37] The O–H deformation vibration is at 1408 cm^{-1}, where the C–OH stretching is at 1227 cm^{-1} and the C–O (epoxy) stretching appears at 1051 cm^{-1}.[38]

Fig. S1A shows the solid state ^{13}C MAS NMR spectrum of GO. The ^{13}C peaks of GO at 62, 73, and 138 ppm, respectively are ascribed to 1, 2-epoxy C-O-C, alcoholic C-OH, and aromatic C=C species which is in agreement with the structural proposal that aromatic rings are one part of the GO structure. The peak at 168 ppm is assigned to the presence of a small amount of carbonyl C=O species present on GO.[39] In order to further investigate the morphology of GO, SEM and TEM measurements are performed. The TEM image reveals the existence of GO as larger sheets having a width of few microns as shown in Fig. 2A. Overlap between the neighboring sheets and slight corrugation are observed due to the large aspect ratio of GO. Distortions are caused by the oxygen groups and the small thickness of the resulting GO sheets lead to a wrinkled topology, as shown in Fig. 2B.

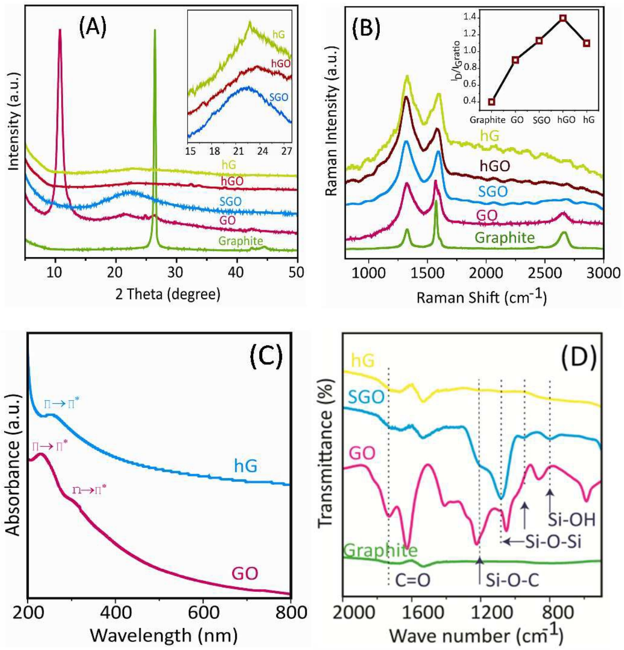

Fig 1: (A) XRD patterns and (B) Raman spectra of graphite, GO and SGO, HGO and HG. Inset of (A) shows the magnified scale for SGO, hGO and hG and inset of (B) shows the I_D/I_G ratio of different samples (C) UV-Visible spectra of GO and hG (D) FT-IR spectra of graphite, GO, SGO and hG

The surface of GO is probed by AFM (Fig. 2I).On an average, the height of GO as measured from the cross section analysis is in the range of >2 to 3 nm. This is indicative of the fact that an exfoliation of graphite down to either one or a maximum of two to three GO nanosheets is achieved. While a pristine graphene sheet is atomically flat with a well-known van der Waals thickness of 0.39 nm, the GO is expected to be thicker (1 nm), mainly owing to the presence of epoxy groups above and below the GO plane.

Graphene silica nanohybrid (SGO)

A negative GO surface favors stronger CTAB-GO interaction. Further, it is known that at alkaline conditions, the surface groups on GO such as –COH and –COOH get deprotonated leaving the GO layer skeleton with negative surface charges (characteristically seen with a large negative zeta potential ~-37 to -40 mV).[40] Accordingly, the synthesized GO sheets are treated with alkali solution (of pH 10) and followed by ultrasonication. When CTAB is added into the GO, a stable colloidal dispersion is formed which is an indication of the zeta potential turning positive as seen in literature.[41] These exfoliated GO sheets are optimally exposed to precursor of silica (TEOS) under basic condition, in such a way that the GO surface gets functionalized with few inorganic silicate layers. The powder XRD pattern in Fig. 1A, GO shows a sharp peak for *002* plane at 10.76° with an associated *d*-spacing of 8.21 Å. As functionalization proceeds, the *002* plane gradually vanishes and a broad peak gradually appears at 22.29° due to the dominant effect of surface silica coating.[42] As shown in Raman spectrum of GO (Fig. 1B), though the peak position of D and G band does not shift due to functionalization, the relative intensities of the D and G bands change considerably and the I_D/I_G ratio increases from 0.9 to 1.14. Increase in D-band intensity suggests that GO has several functional groups attached to its basal plane indicating loss of graphitic nature and the gain of more *sp^3* character. The extent of silica functionalization over the GO surface with respect to the reaction time is further investigated by Raman spectroscopy (Fig. S2). As shown in inset of Fig. S2, I_D/I_G ratio of SGO nanohybrid increases over the course of reaction and after 8 h, there is no further increase in I_D/I_G ratio. The stabilization in the raising I_D/I_G ratio depicts that the maximum surface groups of GO are covered with silicate species.

Covalent bonding of silicate species with GO sheets is identified by two important peaks in FT-IR spectra (Fig. 1D). Followings are the characteristic changes in FT-IR observed during the reaction. A band at 1218 cm^{-1} characteristic of Si–O–C asymmetric stretching appears which is indicative of silica coating on GO surface. On the other hand, the typical carbonyl group band at 1730 cm^{-1} disappears. This proves that the carbonyl groups are converted to Si–O–C bands, as reported in literature.[43] The IR bands due to Si-O-Si and Si-OH framework stretching vibrations are observed in the region of 1078, 940 and 800 cm^{-1}. Solid state ^{29}Si MAS NMR supports this lucidly (Fig. S1B). Solid state ^{29}Si MAS NMR spectrum shows peaks at -90 to -130 ppm due to cross-linked Si-O-Si bonds. A deconvolution process shows the main components to be Q^2 at -89 ppm, Q^3 at -103 ppm and Q^4 at -113 ppm indicating the surface coating of polymerized silica.[44] The noticeable presence of less cross linked Q^2 and Q^3 indicates that the silica coating is not thick. TEM and SEM images of SGO nanohybrid (see Figs. 2C-D) reveal the morphology of 2D sheets that are covered by silica. It is further confirmed by AFM that silica coverage is largely with a thickness of up to 8 nm that shows a few layers of silica cover the GO during the sol-gel process (Figs.2I and 2J).

Holey graphene (hG)

To perforate the GO sheets, the SGO nanohybrids are mixed with 1M NaOH, stirred at room temperature and washed with warm ethanol. The ensuing product is referred as holey graphene oxide (hGO). Electron microscopy images as shown in Figs. 2E and 2F reveal this final product after treatment with NaOH (hGO) exhibits distinct holey structure on GO surface. The hole formation and its enlargement at various stages of alkali treatment have been shown in Fig. S3 through TEM images. A high resolution TEM image as shown in Fig. S4 clearly explains the early stages of hole formation with an average diameter of ~5 nm where lattice fringes of the carbon sheets are also seen. The holes penetrate across the entire thickness of the sheets and form inter-connected net like structure. A hole size distribution histogram (Fig. S5) plotted in the range of few tens to few hundreds of nm shows a clear, mono dispersed average diameter of ~150 nm for the specific concentration of alkali used in the recipe (1M). However, a series of experiments carried out using different alkali concentration reveal that the average diameter can easily be fine-tuned up to a micron. hGO is further reduced by hydrazine hydrate leading to holey graphene (hG) which is considered close to graphene with respect to their properties. The entire process involving conversion of SGO nanohybrid to holey graphene (hG), in presence of NaOH and further reduction by

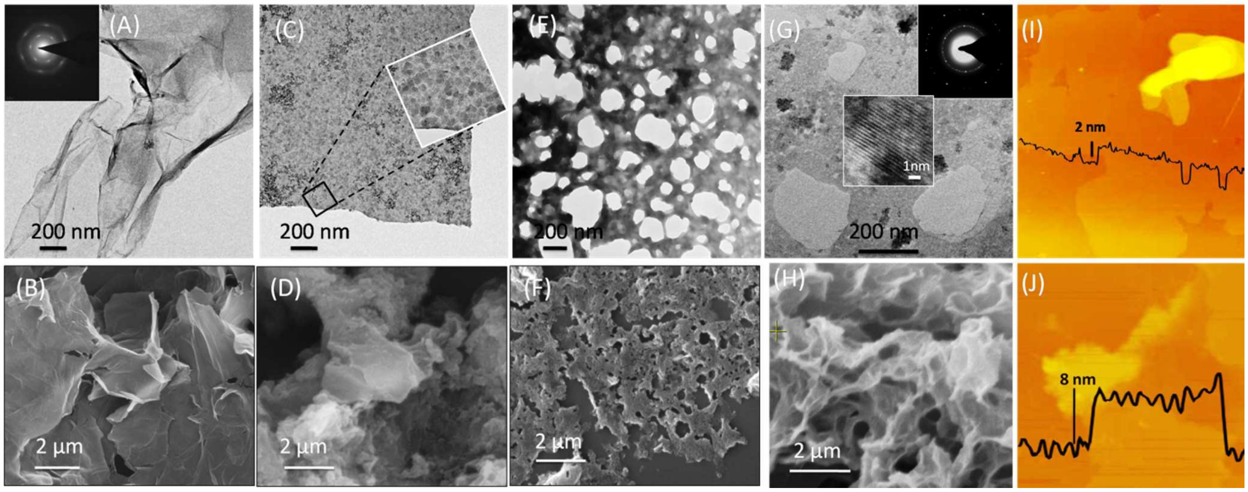

Fig 2: TEM (top) and SEM (bottom) images of GO (A &B), SGO nanohybrid (C&D), hGO (E & F) and hG (G& H); Tapping mode AFM images (last top and bottom) of GO (I) and SGO (J); Insets in 2C and 2G show the enlarged image, HR TEM fringes and SAED image respectively

hydrazine is confirmed by a clear reduction in FWHM of the graphitic peak at 23° as seen in the XRD (Fig. 1A). Due to major degree of structural changes, the Raman spectra of GO, SGO, hGO and hG can be easily differentiated from that of graphite (Fig. 1B). A blue shift in G-line of GO, SGO, hGO and hG with respect to graphite is clearly seen in Fig. 1B. After treatment with NaOH, in hGO sheets, holes become apparent which in turn increases the I_D/I_G ratio of hGO from 1.14 to 1.4. Increase in D band intensity confirms further increase in defect sites than in the case of SGO. After reduction with hydrazine, a sharp decrease in I_D/I_G ratio from 1.4 to 1.1 in hG, proves partial restoration of sp^2 domain sites.

UV-visible absorption spectra (Fig. 1C) for GO and hG show π-π* transition. The restoration of π electronic conjugation in hG by reduction shows up with a red shift in the absorption peak to a longer wavelength (at 257 nm) as compared to GO (230 nm). In addition, GO shows a characteristic shoulder at 300 nm due to n-π* transition which is totally absent in case of hG, confirming the removal of oxygen functionalities from the GO surface. Conversion process of SGO to hG ends with the two major changes in the system; viz., (a) removal of the silica layers from the SGO surface leading to perforation and (b) a reduction to increasing the conductivity of graphene sheets. The main stretching frequencies of GO at 1730 cm^{-1} (C=O stretching) and 3416 cm^{-1} (O-H stretching) are completely removed in hG (Fig. 1D) with emergence of a new band in olefinic, i.e. C=C region. The removal of silica layers from the graphene surface has been confirmed by the complete disappearance of bands at 1218 cm^{-1} (Si-O-C) and 1078 cm^{-1}, 940 cm^{-1} and 800 cm^{-1} (Si-O-Si & Si-OH).

DFT based theoretical analysis

The fact that the present route is simple though efficient, in contrast to the reported routes with compelling need of noble metal/silica nanoparticles for perforation, encouraged us to investigate the process of formation of silica layer and perforation by their removal more closely. Hence, computational studies are carried out in the framework of Density Functional Theory (DFT) as implemented in Gaussian program.[45] Especially, we are interested in understanding the role of alkali treatment on perforation. Silica mineralization at elevated pH is well known. Thus, the top layers of silica can be easily mineralized during the alkali treatment.

However, our interest is to understand the removal of the last few silicate species attached to the graphene surface closely. Accordingly, three models depicting various stages of the reaction are used in the study to understand the process of perforation via sol-gel and an alkali treatment process where (A) Gr-12R is a model with 12 hexagonal rings and represents an rGO/graphene nanoflake; (B) Gr-OSi(OH)$_3$ is a model representing rGO treated with TEOS with a condition where no alkali ions are present; and (C) Gr-OSi(OH)$_2$ONa is model of rGO nanoflake that is functionalized with a silica precursor species and treated with alkali (NaOH). Various computational conditions and their details are available in experimental section (as provided in supplementary).

Fig. S6 shows optimized geometries of (A) Gr-12R, (B) Gr-OSi(OH)$_3$ and (C) Gr-OSi(OH)$_2$ONa. The Figure also gives Mulliken charges on atoms colored (with reference to the color bar representing the charge range of -0.1 to +0.1). The unfunctionalized model, Gr-12R (Fig. S6A) shows a typical charge distribution on the basal plane of graphene/rGO. However, on sol-gel treatment, i.e., when silica species are functionalized on the plane (Fig. S6B), a significant charge polarization within C-C bonds (with dark green C atom as shown encircled, holding a lowest charge of -0.001) vicinal to the functionalized carbon atom is observed.

A convincing although weak non-bonded interaction between a hydroxyl proton and the closest basal carbon is apparently visible through the conspicuous charge difference between the hydroxyl proton (0.465) above the highly polarized (dark green encircled) carbon and the other two hydroxyl protons (0.446 and 0.447). Further, this becomes significantly noticeable in the case of model representing a mild alkaline treated rGO where the H is exchanged with Na (Fig. S6C). Rich electron density of Na perturbs the π cloud over the basal plane as is visible through the polarization of additional C-C bonds around the functionalized C atom (alternative dark green C atoms as encircled in figure having charges ≤0.06). This is, furthermore confirmed by the analysis of total electron density

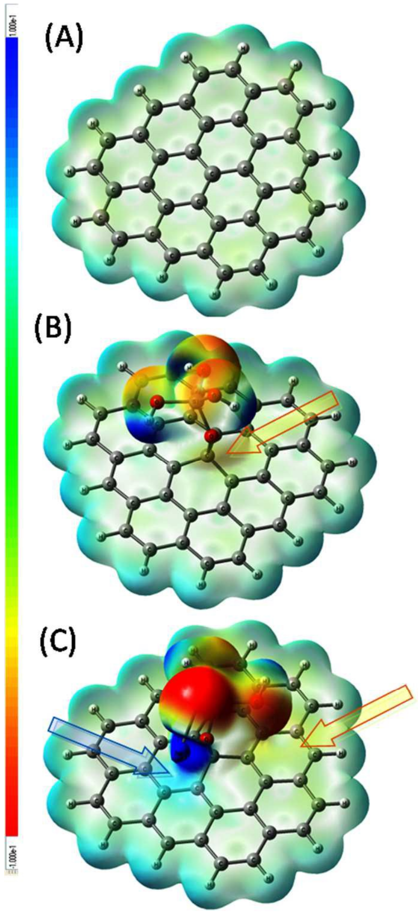

Fig 3: Fade electron density isosurface (isovalue = 0.004) mapped with ESP of (A) Gr-12R, (B) Gr-OSi(OH)$_3$ and (C) Gr-OSi(OH)$_2$ONa depicting potential gradient in the color (common scale bar on left; range = -0.1 to +0.1; red to blue).

isosurfaces generated from the calculated density cubes. The isosurface is mapped with molecular electrostatic potential (MESP) using an isovalue of 0.004 in the potential range of -0.1 to +0.1. The corresponding isosurfaces for Gr-12R (A), Gr-OSi(OH)$_3$ (B) and Gr-OSi(OH)$_2$ONa (C) are shown in Fig. 3. The basal plane without functionalization exhibits a homogeneous distribution of ESP across the sheet as shown in Fig. 3A. A pale greener central region indicates the presence of typical C-C bonds with conjugation while the edge protons showing higher potential with blue color. However, on functionalization with a silica species, the situation changes as seen in Fig. 3B. The significant charge redistribution between the hydroxyl protons and the oxygen atoms shows a strong polarization as also indicated by more red and blue colored regions on them. The diffused reddish yellow region around the functionalized carbon (as indicated by a yellow arrow) shows that the carbon loses a greater density of electrons on functionalization. However, the basal plane is more or less left unaffected as there is no change in color i.e., potential. On the other hand, the alkaline treatment (i.e., Na exchanged with the hydroxyl proton) strongly impacts the ESP of the entire system (Fig. 3C). Deeper red and deeper blue regions on Si(OH)$_3$ONa evidently indicate a greater charge polarization upon the O-Na bond. As a consequence, there is an increased polarization within neighboring hydroxyl bonds as indicated by the increased red and blue colors. This electrostatic imbalance is felt on the basal plane also with noticeable electron delocalization. A blue arrow highlights diffused blue region on the π cloud of the basal plane just beneath the Na atom, is a clear evidence of the stronger charge perturbation. An inductive impact of this is further evident by another diffused reddish yellow region (indicated with a yellow arrow). This makes a clear case of polarization of the conjugation across the first 'C atom circle' around the functionalized carbon on the basal plane. IR vibrational frequencies are calculated to yet again confirm this (Fig S7). Table ST1 shows the most important vibrational frequencies of the C-C bonds. The frequencies of model, Gr-12R (unfunctionalized) are compared with the Gr-OSi(OH)$_2$ONa model (functionalized and alkaline treated). In the later, it is noted that symmetric and asymmetric vibrational modes of skeletal C-C bonds experience a red shift of 4 to 17 cm^{-1} in the finger printing C-C region and up to 34 cm^{-1} in the C=C region. This is a clear sign that alkaline treatment destabilizes the C-C bonds surrounding the functionalized carbon. In conclusion, due to alkali treatment, the C-C bonds are polarized, weaker and more vulnerable for dissociation making way for the silica to carry away several carbon atoms from the basal plane. This as well provides a conclusive clue of how a nanoscopic hole can be created on the carbon plane. More the silica functionalization followed by alkali treatment, higher are the number of holes made thereby enlarging the size of the hole.

Finally, a molecular dynamics (MD) study is carried out on Gr-12R, Gr-OSi(OH)$_3$, and Gr-OSi(OH)$_2$ONa models. The simulations reveal that the inter-atomic distances between the carbon atoms of graphene nanoflakes are higher by about 0.01 Å in case of Gr-OSi(OH)$_2$ONa (alkali treated) as compared to Gr-OSi(OH)$_3$ (untreated with alkali) (Fig. 4)., there by accounting for a lower barrier towards stripping of C-C bonds during the process of hole formation. This further supports the above understanding of the perforation.

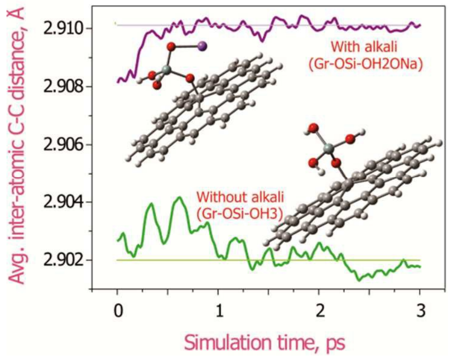

Fig 4: Fluctuations in the inter-atomic distances as simulated through MD calculations for the models depicting rGO/graphene nanoflake with and without alkali treatment.

Electrochemical studies and capacitance measurement

Cyclic voltammetry studies are performed to analyze the capacitance behavior of the hG. The rectangular nature of the curve at varied scan rate of 50, 100, 200 mV/s (Fig. 5A) clearly confirms the capacitive behavior of hG sample, due to the electrochemical double layer (EDL) formation at the interface of electrode and electrolyte. High capacitive behavior of hG is due to the availability of additional in-plane holes on the graphene sheets. These in-plane holes facilitate the electrolyte to easily diffuse across the graphene sheets, which greatly helps in the creation of more EDL layers resulting in higher capacitance. It is interesting to note that there is no obvious distortion even at higher scan rate of 500 mV/s, proving the scope for fast charge/discharge stability and excellent rate capability. The specific capacitance (C_s) is measured using the following equation

$$C_s = 2 \int idV / m\upsilon V \qquad (1)$$

Where C_s is the specific capacitance in F/g, $\int idV$ is the integrated area of the CV curve, m is the mass of the active materials in the single electrode in g, V is the scanned potential window in V, and υ is the scan rate in V/s.

A galvanostatic charge-discharge study is performed to understand the sustainability of the capacitive behavior of hG supercapacitor. The specific capacitance is calculated using the galvanostatic charge-discharge data using the following equation:

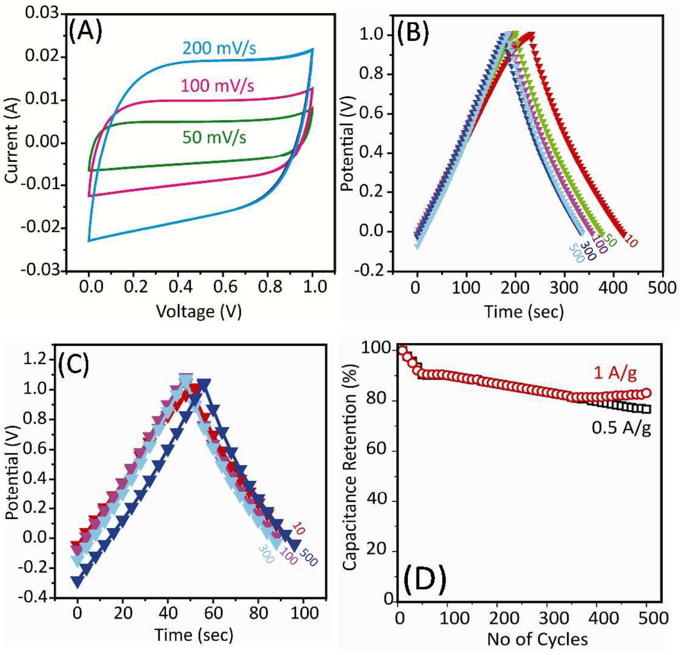

Fig. 5: Performance of holey graphene supercapacitor in 1M H_2SO_4 aqueous electrolyte (A) CV curves obtained using different scan rates (B) Galvanostatic charge/discharge curves at current densities 0.5 A/g and (C) the same at 1A/g (D) cycle life of holey graphene capacitor at current densities 0.5 A/g and 1 A/g.

$$C_s = 2 \times \frac{I}{m\frac{dv}{dt}} \qquad (2)$$

Where C_s is the specific capacitance, I is the current, m is the active mass, and *dv/dt* is the slope obtained from the discharge curve. The charge-discharge plots at different current densities (0.5 A g^{-1} and 1 A g^{-1}) are shown in Figs. 5B-C. The highest specific capacitance value 250 F g^{-1} is obtained at a current density of 0.5 A g^{-1}. It is seen from the graph that as the current density increases, the specific capacitance slightly decreases, due to the obvious diffusional limitations of the active ions on the electrode surface at higher scan rates. To compare the actual impact of perforation on the gain in capacitance, the charge-discharge characteristics of rGO is collected and compared with that of hG. Fig. S8 of ESI shows a charge-discharge comparison plot between hG and rGO under identical conditions. While hG shows C_s of 250 F g^{-1} at 0.5 A g^{-1} the unperforated rGO shows C_s of only 90.9 F g^{-1} at the same current density. Table ST2 provides a general comparison of our material with various supercapacitor materials prepared using other conventional routes especially where alkali treatment is used.[S5-S8] It is clearly evident that our route produces better performing material at truly ambient and at aqueous conditions and that the nanoperformation increases the capacitance by 2.5 times. It is important to note that these values correspond to the bare graphene sheet without any functionalization. A stability testing is also done up to 500 cycles at different current densities viz., 0.5 A g^{-1} and 1 A g^{-1} (Fig. 5D). Even after 500 cycles, up to 80 % and 85 % capacitance value retention, at current density 0.5 A g^{-1}, 1.0 A g^{-1}, respectively are observed. The better electrochemical performances of the hG electrode can be ascribed of its unique morphology and surface chemistry as described below. Firstly, the functionalization efficiently inhibits the restacking of graphene sheets by being as “spacer” during the process. Secondly, it produces numerous holes and “footprints” (Fig. 2E-H) on the surface of sheets on its removal. The “footprints”, reported in literature[46] as the fresh crumples, which can act as ion-buffering reservoirs that greatly facilitate the fast transportation of electrolyte ions to the internal surfaces while the holes act as ion passage for the electrolyte to easily diffuse between the graphene sheets.

Dye adsorption

A systemic analysis of dye adsorption behavior of GO, SGO, hGO and hG towards Rhodamine B (RhB) are shown in Fig. 6. It is distinctly evident that hG has higher adsorption capacity than GO, hGO and SGO. The adsorption capacity (Q_e) values are calculated by using the following equation[47]

$$Q_e = (C_0 - C_e)V/M \qquad (3)$$

Where C_0 is the initial concentration of RhB (mg L^{-1}), C_e is the concentration of residual RhB solution after adsorption (mg L^{-1}), V stands for the volume of the solution (L) and M is the mass of the adsorbent (g). As shown in Fig. 6, hG exhibits the highest adsorption capacity (for RhB) which is up to 58.8 mg g^{-1}. In principle, the interaction between RhB and carbon surface can be through three ways, (i) physisorption (ii) binding through surface oxygen groups and (iii) π-π^* conjugation through sp^2 carbon. Here, oxygen groups could not be the reason since the adsorption capacity is well preserved and enhanced in the reduced sample (hG) where oxygen groups are extremely extinct. It is interesting to note that hG has higher adsorption capacity for RhB than many reported adsorbents including GO and rGO.[48,49] The adsorption capacity of the hG is better compared to several reported carbon based adsorbents. Superior sorption properties of hG for the dye can be attributed to the following unique features available with the hG, unlike with the traditional carbon sorbents, viz., (a) in addition to the inherent high surface area of nanoscopic hG sheets, large space is available between the sheets for possible dye confinement, a general observation in the case of thin 2D sheets of high aspect ratio being organized in 3D space and (b) a number of unsaturated atoms along the edges of the holes created on the hG sheets are available as chemically reactive and strong adsorption sites that are naturally more preferred by organic molecules with conjugations such as RhB dye.[50] Few adsorbents (Table ST3)[S9-S12] show better adsorption capacities, however their synthesis routes are not as easy i.e., in ambient conditions especially for large scale production. Hence, the present route of producing the hG is highly promising for industrial level production and further applications.

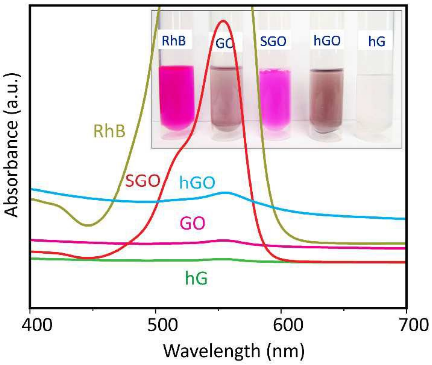

Fig. 6: UV-Vis spectra of the original RhB dye solution and after different adsorbent treatment: SGO, hGO, GO and hG respectively; inset is the corresponding photographs

Conclusions

In summary, for the first we report a simple and inexpensive route to perforate graphene without the requirement of a template or hazardous acids. Holey graphene is made via a simple sol-gel process to coat the surface with thin silica layers followed by their removal through a mild alkali treatment. The hole diameter can be controlled by simply varying the concentration of the treated alkali solution. The entire synthesis is scalable in an aqueous and at perfect ambient conditions that attracts researchers with the advent of no use of harmful chemical/solvent for safe large scale production. Electrochemical testing of the hG for supercapacitor demonstrates its high specific capacitance (250 F g^{-1}) at 0.5 A g^{-1} retainable up to several hundreds of charge/discharge cycles. The hG also shows a good adsorption for organic pollutants (58.8 mg g^{-1} with RhB dye) displaying the availability of large and active internal surface area. These are attributed to the introduction of enormous in-plan holes in the graphene sheets that dramatically enhances the cross plane diffusion of electrolytes/ions leading to superior capacitance. Similarly, as the nano-perforation increases unsaturation on the basal plane, it facilitates the interaction between the highly porous and networked surface of hG and molecules such as RhB with conjugation as observed on a revealing dye adsorption study. A systematic DFT based study provides interesting insight with clues on various molecular events and forces possibly involved in the perforation process and the hole size control. The strong non-bonded electrostatic interaction between the alkali substituted silica species and the graphene plane explains the possible removal of large number of carbon atoms leading the perforation. The major innovation of this strategy is that perforation of the graphene sheet can be much easier through minimized functionalization with thinner layers of inorganic species that require less effort (not requiring strong acids) to remove them.

Acknowledgements

SKJ acknowledges the CSIR, New Delhi for a fellowship. This research work is supported by the grants under OLP002626 (CSIR-EMPOWER project) and MLP029226. Mr. Gaurav Sudhir Lole is acknowledged for help in TEM. The authors acknowledge the Center of Excellence in Scientific Computing (CoESC) at CSIR-National Chemical Laboratory (NCL), Pune for access to its high performance computing clusters.

References

1 K. S. Novoselov, A. K. Geim, S. V. Morozov, D. Jiang, Y. Zhang, S. V. Dubonos, I. V. Grigorieva and A. A. Firsov, *Science*, 2004, **306**, 666.
2 S. V. Morozov, K. S. Novoselov, M. I. Katsnelson, F. Schedin, D. C. Elias, J. A. Jaszczak and A. K. Geim, *Phys. Rev. Lett.*, 2008, **100**, 016602.
3 X. Du, I. Skachko, A. Barker and E. Y. Andrei, *Nat. Nano.*, 2008, **3**, 491.
4 T. J. Booth, P. Blake, R. R. Nair, D. Jiang, E. W. Hill, U. Bangert, A. Bleloch, M. Gass, K. S. Novoselov, M. I. Katsnelson and A. K. Geim, *Nano Lett.*, 2008, **8**, 2442.
5 Z. Dong, C. Jiang, H. Cheng, Y. Zhao, G. Shi, L. Jiang and L. Qu, *Adv. Mater.*, 2012, **24**, 1856.
6 K. S. Novoselov, A. K. Geim, S. V. Morozov, D. Jiang, Y. Zhang, S. V. Dubonos, I. V. Grigorieva and A. A. Firsov, *Science*, 2004, **306**, 666.
7 K. S. Kim, Y. Zhao, H. Jang, S. Y. Lee, J. M. Kim, K. S. Kim, J.-H. Ahn, P. Kim, J.-Y. Choi and B. H. Hong, *Nature*, 2009, **457**, 706.
8 Y. Hernandez, V. Nicolosi, M. Lotya, F. M. Blighe, Z. Sun, S. De, I. T. Mc Govern, B. Holland, M. Byrne, Y. K. Gun'Ko, J. J. Boland, P. Niraj, G. Duesberg, S. Krishnamurthy, R. Goodhue, J. Hutchison, V. Scardaci, A. C. Ferrari and J. N. Coleman, *Nat. Nano.*, 2008, **3**, 563.

9 S. Stankovich, D. A. Dikin, R. D. Piner, K. A. Kohlhaas, A. Kleinhammes, Y. Jia, Y. Wu, S. T. Nguyen and R. S. Ruoff, *Carbon*, 2007, **45**, 1558.
10 S. Park and R. S. Ruoff, *Nat. Nano.*, 2009, **4**, 217.
11 D. Li, M. B. Muller, S. Gilje, R. B. Kaner and G. G. Wallace, *Nat. Nano.*, 2008, **3**, 101.
12 X. Zhao, C. M. Hayner, M. C. Kung and H. H. Kung, *ACS Nano*, 2011, **5**, 8739.
13 D. R. Dreyer, S. Park, C. W. Bielawski and R. S. Ruoff, *Chem. Soc. Rev.*, 2010, **39**, 228.
14 G. K. Ramesha and S. Sampath, *Electroanalysis*, 2007, **19**, 2472.
15 J. Zhang, F. Zhao, Z. Zhang, N. Chen and L. Qu, *Nanoscale*, 2013, **5**, 3112.
16 B. G. Choi, M. Yang, W. H. Hong, J. W. Choi and Y. S. Huh, *ACS Nano*, 2012, **6**, 4020.
17 Y. Ito, Y. Tanabe, H. J. Qiu, K. Sugawara, S. Heguri, N. H. Tu, K. K. Huynh, T. Fujita, T. Takahashi, K. Tanigaki and M. Chen, *Angew. Chem. Int. Ed.*, 2014, **53**, 4822.
18 X.-C. Dong, H. Xu, X.-W. Wang, Y.-X. Huang, M. B. Chan-Park, H. Zhang, L.-H. Wang, W. Huang and P. Chen, *ACS Nano*, 2012, **6**, 3206.
19 Z.-S. Wu, Y. Sun, Y.-Z. Tan, S. Yang, X. Feng and K. Müllen, *J. Am. Chem. Soc.*, 2012, **134**, 19532.
20 S. H. Lee, H. W. Kim, J. O. Hwang, W. J. Lee, J. Kwon, C. W. Bielawski, R. S. Ruoff and S. O. Kim, *Angew. Chem. Int. Ed.*, 2010, **49**, 10084.
21 C. Liang, Z. Li and S. Dai, *Angew. Chem. Int. Ed.*, 2008, **47**, 3696.
22 T. Kyotani, *Carbon*, 2000, **38**, 269.
23 S. Patchkovskii, J. S. Tse, S. N. Yurchenko, L. Zhechkov, T. Heine and G. Seifert, *Proc. Natl. Acad. Sci. USA*, 2005, **102**, 10439.
24 D.-e. Jiang, V. R. Cooper and S. Dai, *Nano Lett.*, 2009, **9**, 4019.
25 J. Zhu, D. Yang, X. Rui, D. Sim, H. Yu, H. E. Hoster, P. M. Ajayan and Q. Yan, *Small*, 2013, **9**, 3390.
26 A. Du, Z. Zhu and S. C. Smith, *J. Am. Chem. Soc.*, 2010, **132**, 2876.
27 J. Bai, X. Zhong, S. Jiang, Y. Huang and X. Duan, *Nat. nano.*, 2010, **5**, 190.
28 O. Akhavan, *ACS Nano*, 2010, **4**, 4174.
29 Z. Zeng, X. Huang, Z. Yin, H. Li, Y. Chen, H. Li, Q. Zhang, J. Ma, F. Boey and H. Zhang, *Adv. Mater.*, 2012, **24**, 4138.
30 M. Wang, L. Fu, L. Gan, C. Zhang, M. Rümmeli, A. Bachmatiuk, K. Huang, Y. Fang and Z. Liu, *Sci. Rep.*, 2013, **3**, 1238.
31 J. G. Radich and P. V. Kamat, *ACS Nano*, 2013, **7**, 5546.
32 Y. Lin, K. A. Watson, J.-W. Kim, D. W. Baggett, D. C. Working and J. W. Connell, *Nanoscale*, 2013, **5**, 7814.
33 D. Mhamane, A. Suryawanshi, S. M. Unni, C. Rode, S. Kurungot and S. Ogale, *Small*, 2013, **9**, 2801.
34 W. L. Zhang, B. J. Park and H. J. Choi, *Chem. Comm.*, 2010, **46**, 5596.
35 L. Kou and C. Gao, *Nanoscale*, 2011, **3**, 519.
36 P. Huang, C. Xu, J. Lin, C. Wang, X. Wang, C. Zhang, X. Zhou, S. Guo and D. Cui, *Theranostics*, 2011, **1**, 240.
37 T. Szabó, O. Berkesi, P. Forgó, K. Josepovits, Y. Sanakis, D. Petridis and I. Dékány, *Chem. Mater.*, 2006, **18**, 2740.
38 D. Li, M. B. Muller, S. Gilje, R. B. Kaner and G. G. Wallace, *Nat. Nano.*, 2008, **3**, 101.
39 Y. Li, H. Chen, L. Y. Voo, J. Ji, G. Zhang, G. Zhang, F. Zhang and X. Fan, *J. Mater. Chem.*, 2012, **22**, 15021.
40 Z.-M. Wang, W. Wang, N. Coombs, N. Soheilnia and G. A. Ozin, *ACS Nano*, 2010, **4**, 7437.
41 M. Zhang, Y. Wu, X. Feng, X. He, L. Chen and Y. Zhang, *J. Mate. Chem.*, 2010, **20**, 5835.
42 X. Guo, X. Liu, B. Xu and T. Dou, *Colloids and Surfaces A: Physicochem. Eng. Aspects*, 2009, **345**, 141.
43 K. G. Lee, R. Wi, M. Imran, T. J. Park, J. Lee, S. Y. Lee and D. H. Kim, *ACS Nano*, 2010, **4**, 3933.
44 Z. M. Wang, K. Hoshinoo, K. Shishibori, H. Kanoh and K. Ooi, *Chem. Mater.*, 2003, **15**, 2926.
45 M. J. Frisch, G. W. Trucks, H. B. Schlegel, G. E. Scuseria, M. A. Robb, J. R. Cheeseman, G. Scalmani, V. Barone, B. Mennucci, G. A. Petersson, H. Nakatsuji, M. Caricato, X. Li, H. P. Hratchian, A. F. Izmaylov, J. Bloino, G. Zheng, J. L. Sonnenberg, M. Hada, M. Ehara, K. Toyota, R. Fukuda, J. Hasegawa, M. Ishida, T. Nakajima, Y. Honda, O. Kitao, H. Nakai, T. Vreven, J. A. Montgomery Jr., J. E. Peralta, F. Ogliaro, M. J. Bearpark, J. Heyd, E. N. Brothers, K. N. Kudin, V. N. Staroverov, R. Kobayashi, J. Normand, K. Raghavachari, A. P. Rendell, J. C. Burant, S. S. Iyengar, J. Tomasi, M. Cossi, N. Rega, N. J. Millam, M. Klene, J. E. Knox, J. B. Cross, V. Bakken, C. Adamo, J. Jaramillo, R. Gomperts, R. E. Stratmann, O. Yazyev, A. J. Austin, R. Cammi, C. Pomelli, J. W. Ochterski, R. L. Martin, K. Morokuma, V. G. Zakrzewski, G. A. Voth, P. Salvador, J. J. Dannenberg, S. Dapprich, A. D. Daniels, Ö. Farkas, J. B. Foresman, J. V. Ortiz, J. Cioslowski and D. J. Fox, Gaussian 09, Revision D.01, Gaussian, Inc., Wallingford CT, 2009
46 J. Yan, Q. Wang, T. Wei, L. Jiang, M. Zhang, X. Jing and Z. Fan, *ACS Nano*, 2014, **8**, 4720.
47 Z. Dong, D. Wang, X. Liu, X. Pei, L. Chen and J. Jin, *J. Mater. Chem. A*, 2014, **2**, 5034.
48 H. Ren, D. D. Kulkarni, R. Kodiyath, W. Xu, I. Choi and V. V. Tsukruk, *ACS Appl. Mater. Interfaces*, 2014, **6**, 2459.
49 Z. Geng, Y. Lin, X. Yu, Q. Shen, L. Ma, Z. Li, N. Pan and X. Wang, *J. Mate. Chem.*, 2012, **22**, 3527.
50 M. Petravic, R. Peter, I. Kavre, L. H. Li, Y. Chen, L.-J. Fan and Y.-W. Yang, *Phys. Chem. Chem. Phys.*, 2010, **12**, 15349.